Synergistic Modulation of Electronic Interaction to Enhance Intrinsic Activity and Conductivity of Fe–Co–Ni Hydroxide Nanotube for Highly Efficient Oxygen Evolution Electrocatalyst

Huanfeng Huang, Shunlian Ning, Yanyu Xie, Zhujie He, Jun Teng, Zhuodi Chen, Yanan Fan, Jian-ying Shi, Mihail Barboiu, Dawei Wang, et al.

Synergistic modulation of electronic interaction to enhance intrinsic activity and conductivity of Fe–Co–Ni hydroxide nanotube for highly efficient oxygen evolution electrocatalyst

Huanfeng Huang, Shunlian Ning, Yanyu Xie, Zhujie He, Jun Teng, Zhuodi Chen, Yanan Fan, Jian-Ying Shi, Mihail Barboiu, Dawei Wang,* and Cheng-Yong Su

H. Huang, Y. Xie, S. Ning, J. Teng, Z. He, Z. Chen, Y. Fan, Prof. J.-Y. Shi, Prof. M. Barboiu, Prof. D. Wang, Prof. C.-Y. Su
Lehn Institute of Functional Materials, School of Chemistry
MOE Laboratory of Bioinorganic and Synthetic Chemistry
Sun Yat-Sen University
Guangzhou 510275, China
E-mail: wdawei@mail.sysu.edu.cn

Prof. M. Barboiu
Adaptive Supramolecular Nanosystems Group
Institut Europeen des Membranes
University of Montpellier
ENSCM-CNRS
Place E. Bataillon CC047
34095 Montpellier, France

The large-scale hydrogen production and application through electrocatalytic water splitting depends crucially on the development of highly efficient, cost-effective electrocatalysts for oxygen evolution reaction (OER), which, however, remains challenging. Here, we develop a new electrocatalyst of trimetallic Fe–Co–Ni hydroxide (denoted as $FeCoNiO_xH_y$) with nanotubular structure through enhanced Kirkendall process under applied potential. The $FeCoNiO_xH_y$ features synergistic electronic interaction between Fe, Co, and Ni, which not only notably increases the intrinsic OER activity of $FeCoNiO_xH_y$ by facilitating the formation of *OOH intermediate, but also substantially improves the intrinsic conductivity of $FeCoNiO_xH_y$

to facilitate charge transfer and activate catalytic sites through electrocatalyst by promoting the formation of abundant Co^{3+}. Therefore, $FeCoNiO_xH_y$ delivers remarkably accelerated OER kinetics and superior apparent activity, indicated by an ultra-low overpotential potential of 257 mV at a high current density of 200 mA cm^{-2}. Our work is of fundamental and practical significance for synergistic catalysis related to advanced energy conversion materials and technologies.

1. Introduction

Development of renewable energy conversion technologies and materials is an effective way to alleviate the ever-increasing global energy and environmental crisis.[1-3] As one of the most promising and clean energy sources, hydrogen (H_2) can be produced by water splitting with electric and/or solar energy input.[4, 5] For electrocatalytic water splitting, large overpotential is required due to the sluggish kinetics of the anodic four-electron-involved oxygen evolution reaction (OER).[6] Therefore, active and earth-abundant OER electrocatalysts are highly desirable to achieve efficient and cost-effective water splitting for the large-scale hydrogen production and application. The oxides, hydroxides, and oxyhydroxides of transition metals, typically Fe, Co and Ni, have been regarded as promising candidates for OER electrocatalysts under alkaline conditions, due to their moderate activity, good stability, ready availability, and low cost.[6-8] Recent experimental and theoretical studies imply that Fe, Co, and Ni feature distinct electrochemical natures in OER, and appropriate integration of these metals to induce synergistic effect in multicomponent electrocatalysts can leads to enhanced OER activity.[9-11]

Typically, the mechanism of OER under alkaline condition can be interpreted as a sequential conversion process of adsorbed OH$^-$ into oxygenated intermediates of *OH, *O, *OOH, and finally to O_2.[1, 11] Accordingly, the intrinsic activity of Fe-, Co-, and/or Ni-based multicomponent electrocatalysts can be enhanced by inducing synergistic effect on the adsorption, stabilization, and/or generation of these oxygenated intermediates. For instance, Fe in bimetallic NiFe and CoFe layered double hydroxides (LDHs) shows flexible electronic structure and synergy with nearest-neighbor M (M = Ni or Co) by forming O-bridged Fe–M reaction centers, which benefit the stabilization of *O intermediate and thus account fundamentally for high catalytic activity (348 and 404 mV overpotential for NiFe and and CoFe LDH, respectively, at a current density of 10 mA cm^{-2}).[12] Furthermore, Fe and Ni in bimetallic (Fe,Ni)OOH facilitate the formation of *O and *OOH, respectively, and the synergy between Fe and Ni also results in optimal OER performance (300–400 mV overpotential at 10 mA cm$^-$^{2}).[13] The intrinsic activity of Fe-, Co-, and/or Ni-based multicomponent electrocatalysts can

2

be further enhanced by coupling the intermediate adsorption/stabilization/generation modulation with vacancy, coordination, and/or structure engineering so as to achieve notably decreased overpotentials (230–270 mV).[14-17]

In addition to intrinsic activity, the intrinsic electrical conductivity of Fe-, Co-, and/or Ni-based multicomponent electrocatalysts may also be improved, which facilitates the transfer of charge carriers between electrode, electrocatalysts and adsorbed intermediates, and thus leads to accelerated OER kinetics and enhanced apparent activity of electrocatalysts.[18] Increased intrinsic conductivity also allows for the efficient activation of all catalytic sites throughout multicomponent electrocatalysts, and thus effectively diminishes the disadvantages of thickness-dependent OER activity observed when electrocatalyst conductivity is improved solely by using conductive supports.[19, 20] As a representative example, Fe oxyhydroxide usually shows high overpotential (low apparent activity) despite its high intrinsic activity, which is attributed to its poor conductivity; in sharp contrast, Fe within conductive scaffold of Ni or Co oxyhydroxides can be efficiently activated so as to deliver much lower overpotentials (high apparent activity).[19, 21, 22] Moreover, the OER activity of Fe-, Co-, and/or Ni-based multicomponent electrocatalysts could be further improved by simultaneous enhancement in their intrinsic activity and conductivity. In a recent work, trimetallic FeCoNi–LDH shows excellent OER activity (269 mV at 10 mA cm^{-2}), which results from the collective contribution of increased quantity and activity of catalytic sites, decreased charge transfer resistance as well as improved hydrophilicity upon the addition of Fe.[23]

Despite recent progress, the simultaneous regulation of intrinsic activity and conductivity in Fe-, Co-, and/or Ni-based multicomponent electrocatalysts remains very challenging, particularly for trimetallic FeCoNi electrocatalysts due to their complex electrochemical natures and electronic interactions. In many cases, Fe in multicomponent electrocatalysts shows stabilization effect on Co and/or Ni, which greatly suppresses the oxidation of Co and/or Ni to higher oxidation states under OER condition, and thus hinders the formation of sufficiently conductive Co and/or Ni oxyhydroxides for Fe to deliver its high intrinsic activity.[21, 24, 25]

Here, we develop a new electrocatalyst of trimetallic Fe- and Co-doped Ni hydroxide (denoted as FeCoNiO$_x$H$_y$) with nanotubular structure, which was synthesized through an enhanced Kirkendall process of a Fe-, Co-, and Ni-containing metal-organic framework (MOF) under applied potential and alkaline condition (**Scheme 1**a,b). The FeCoNiO$_x$H$_y$ features synergistic electronic interaction between Fe, Co, and Ni, which not only notably increases the intrinsic OER activity of FeCoNiO$_x$H$_y$ by substantially decreasing the Gibbs free energy for the formation of *OOH intermediate, the rate-determining step (RDS) of OER, but also ramarkably

3

enhances the intrinsic conductivity of $FeCoNiO_xH_y$ to significantly facilitate the charge transfer and catalytic site activation throughout electrocatalyst by promoting the formation of abundant Co^{3+} (Scheme 1c). In such a way, the high intrinsic OER activity of Fe^{3+} and high electrical conductivity of Co^{3+} are properly integrated in $FeCoNiO_xH_y$. The collaborative coupling of significantly enhanced intrinsic activity and conductivity leads to remarkably accelerated OER kinetics at low potential and superior apparent activity of $FeCoNiO_xH_y$, indicated by an ultra-low overpotential potential of 257 mV at a great current density of 200 mA cm^{-2} in 1 M KOH solution. These results are of fundamental and practical significance for synergistic catalysis related to advanced energy conversion materials and technologies.
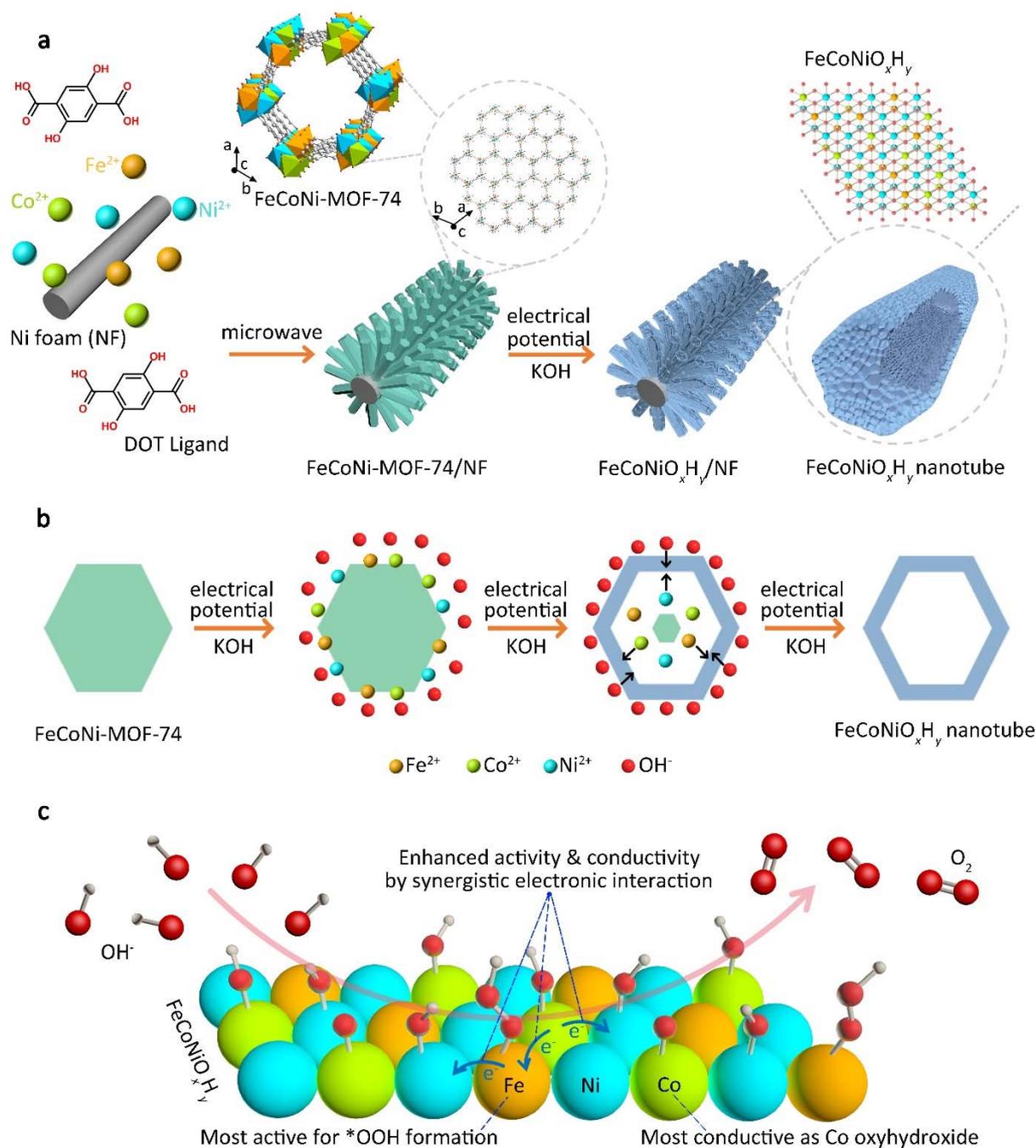
Scheme 1. (a) Illustration of the synthesis of NF-supported FeCoNiO$_x$H$_y$ nanotubes from FeCoNi-MOF-74/NF. (b) Proposed formation process of FeCoNiO$_x$H$_y$ nanotubes. (c) Proposed synergistic electronic interaction in FeCoNiO$_x$H$_y$ for highly efficient OER.

2. Results and Discussion

MOF-74 with one dimensional channel structure is assembled from 2,5-dihydroterephalic acid (DOT; as ligand) and metal node, in which metal ions of Fe, Co, an Ni with different ionic radii can be uniformly integrated into homogeneous, single-phase structures and readily adjusted (Scheme 1a).[26, 27] Hexagonal nanorods of FeCoNi-MOF-74 supported on nickel foam (denoted

5

as FeCoNi-MOF-74/NF) were synthesized via a one-step synthetic procedure (Scheme 1a, Figure S1, and Table S1),[28] in which NF acted not only the support but also the source of Ni^{2+} for the formation of trimetallic FeCoNi-MOF-74.[29-31] As shown in the images from scanning electron microscope (SEM) and transmission electron microscope (TEM) in **Figure 1**a,b, the FeCoNi-MOF-74 hexagonal nanorods show smooth surfaces, solid interior, 80–270 nm in diameter, and 0.3–1.0 μm in length. The energy-dispersive spectroscopy (EDX) area maps indicate the homogeneous distribution of Fe, Co, and Ni in FeCoNi-MOF-74 (Figure 1c and Figure S2), and the line scans confirm the solid nature of FeCoNi-MOF-74 nanorod (Figure 1d). Moreover, the Fe:Co:Ni atomic ratio is quantified to be 0.59:0.63:1 by inductively coupled plasma-atomic emission spectroscopy (ICP-AES; Table S2). The formation of trimetallic FeCoNi-MOF-74 is further confirmed by its power X-ray diffraction (PXRD) pattern, which agrees well with the simulated one (Figure 1k).
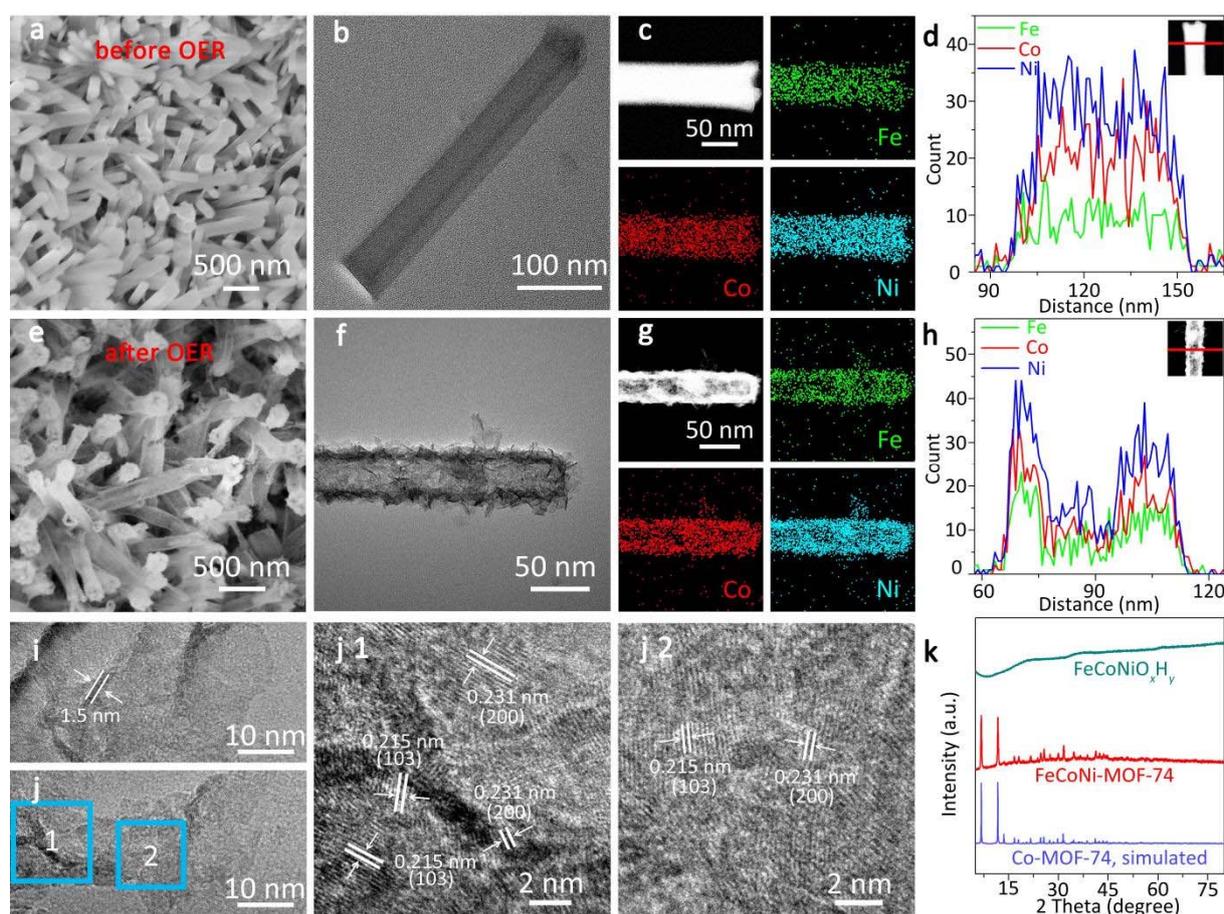
Figure 1. Electron microscopy characterization of (a–d) FeCoNi-MOF-74 and (e–j) FeCoNiO$_x$H$_y$. (a, e) SEM images, (b, f) TEM images, (c, g) EDX element mapping, (d, h) EDX line scans, and (i, j) HRTEM images. (k) PXRD patterns.

The FeCoNi-MOF-74 nanorods were treated with an *in situ* electrochemical oxidation process at a potential window of 1.0–1.6 V vs. reversible hydrogen electrode (RHE) in 1 M KOH solution (cf. Scheme 1a and Figure S3, and also experimental details in Supporting Information). After electrochemical oxidation, the size of each nanorod does not change notably (70–300 nm in diameter and 0.3–1.1 μm in length; Figure 1e), but its surface becomes rough. Interestingly, TEM image, EDX element maps and line scans reveal that the solid nanorod of FeCoNi-MOF-74 are converted into tubular nanostructures (nanotubes) consisted of ultra-thin nanosheets (Figure 1f–h), and Fe, Co, and Ni still distribute homogeneously in each nanotube (Figure 1f,g). The Fe:Co:Ni atomic ratio in nanotubes is determined to be 0.30:0.48:1 by ICP-AES (Table S2), which indicates a decreased content of Fe and Ni and thus suggests a loss of Fe and Ni during the electrochemical oxidation process. Moreover, high-resolution TEM (HRTEM) images of the ultra-thin nanosheets in a nanotube show that the nanosheets are *ca.* 1.5 nm in thickness and feature a poor crystallinity nature (Figure 1i,j), indicated by the large amorphous region embedded with ultrasmall crystalline grains (2–6 nm). The poor crystallinity nature of our product is further confirmed by its PXRD pattern, which hardly show any characteristic diffraction peaks. To check out the composition of our product, the ultrasmall crystalline grains in a nanosheet were observed at a much higher magnification with HRTEM, which shows two set of plane spacing of 0.215 and 0.231 nm (Figure 1j) corresponding to the (103) and (200) plane of hydrated nickel hydroxide (JCPDS#22–0444), respectively.[32] The selected-area electron diffraction (SAED) pattern of our product also presents two sets of weak concentric rings that correspond to the (103) and (300) plane of hydrated nickel hydroxide, respectively (Figure S4). The above results thus collectively suggest that our product consists of Fe- and Co-doped hydrated nickel hydroxide (FeCoNiO$_x$H$_y$). Moreover, as demonstrated in our early work, the large amorphous region embedded with abundant ultrasmall crystalline grains in FeCoNiO$_x$H$_y$ should result in large and hierarchical porosity that benefits the mass transfer and active site exposure during OER.[33] Indeed, N$_2$-sorption measurements imply that FeCoNiO$_x$H$_y$ have a large Brunauer-Emmett-Teller (BET) surface area of 111 m^2 g^{-1} and hierarchical pores with size ranging from 1.2 to 9.0 nm (Figure S5–8).

The conversion of solid FeCoNi-MOF-74 nanorods into FeCoNiO$_x$H$_y$ nanotubes could be rationalized by the Kirkendall effect (Scheme 1b).[34] Briefly, due to the instability of FeCoNi-MOF-74 in concentrated KOH electrolyte, the ions of Fe, Co, and Ni are released from the decomposed surface of FeCoNiMOF-74 nanorods and react with OH$^-$ from electrolyte to produce a shell layer of FeCoNiO$_x$H$_y$, which then acts as a template/backbone for the deposition of subsequently formed FeCoNiO$_x$H$_y$.[35] The formation of FeCoNiO$_x$H$_y$ shell layer results in a

7

depletion of local metal ions and OH⁻, which in turn leads to the outward diffusion of freshly released metal ions from inner, decomposed FeCoNiMOF-74 and the inward diffusion of OH⁻ from outer electrolyte. Eventually, all the fresh FeCoNiO$_x$H$_y$ are formed and deposited on the surface of previously generated FeCoNiO$_x$H$_y$, leading to the complete decomposition of FeCoNiMOF-74 and the formation of FeCoNiO$_x$H$_y$ nanotubes (Figure S9). It is worth noting that in concentrated KOH electrolyte, the applied high potential not only greatly promotes the decomposition of FeCoNiMOF-74, but also notably accelerates the directional diffusion of metal ions and OH⁻, leading an enhanced Kirkendall process and finally the rapid formation of FeCoNiO$_x$H$_y$ with poor crystallinity nature but well-defined, compact nanotubular structure (Figure 1e–k).[33] In contrast, under no potential but otherwise identical conditions, the reaction process could be much slower, thus resulting a product (denoted as FeCoNi-MOF-74-KOH/NF) with improved crystallinity but ill-defined, loose nanotubular structure (Figure S10–14). As unambiguously indicated by the characteristic PXRD peaks (Figure S10), concentric electron diffraction rings (Figure S11), and lattice fringes (Figure S12), FeCoNi-MOF-74-KOH/NF can be assigned to FeCoNi-LDH, in line with literature reports.[23, 31]

The electrocatalytic OER activities of FeCoNiO$_x$H$_y$/NF with various Fe:Co:Ni ratios (Figure S15–19) were evaluated and optimized by linear scanning voltammetry (LSV) that was operated at a scan rate of 2 mV s⁻¹ in a three-electrode electrochemical cell with an aqueous solution of 1 M KOH as electrolyte (**Figure 2**a,b). At a current density of 10 mA cm⁻², Fe$_{0.5}$Co$_{0.5}$NiO$_x$H$_y$/NF with an ICP-AES-based precise Fe:Co:Ni atomic ratio of 0.3:0.48:1 delivers the best performance (for simplification, Fe$_{0.5}$Co$_{0.5}$NiO$_x$H$_y$ is specifically referred to FeCoNiO$_x$H$_y$, and the other control samples of trimetallic electrocatalysts are denoted as FeCoNiO$_x$H$_y$ with their Fe:Co:Ni feed ratios as subscripts), indicated by an overpotential of 216 mV and a Tafel slope of 32 mV dec⁻¹, which is notably superior to the commercially available benchmark OER electrocatalyst of RuO₂ supported on NF (overpotential of 267 mV and Tafel slope of 49 mV dec⁻¹). Moreover, at a much higher current density of 200 mA cm⁻², the optimized FeCoNiO$_x$H$_y$/NF further shows an ultra-low overpotential of 257 mV, while the benchmark OER electrocatalyst of RuO₂/NF can only deliver a much higher overpotential of 323 mV at a much lower current density of 100 mA cm⁻². The much lower overpotential and Tafel slope indicate that FeCoNiO$_x$H$_y$/NF is capable of delivering remarkable electrocatalytic activity and fast reaction kinetics toward OER. In fact, such remarkable electrocatalytic performance enables FeCoNiO$_x$H$_y$/NF to be among the best Fe-, Co- and/or Ni-based bi- and/or trimetallic OER electrocatalysts developed recently (Table S3). The durability of FeCoNiO$_x$H$_y$/NF is also confirmed by the chronoamperometric test at a constant overpotential

(corresponding to a current density of 10 and 200 mA cm^{-2}, respectively), during which the current density can be well retained for up to 24 h (Figure 2d).
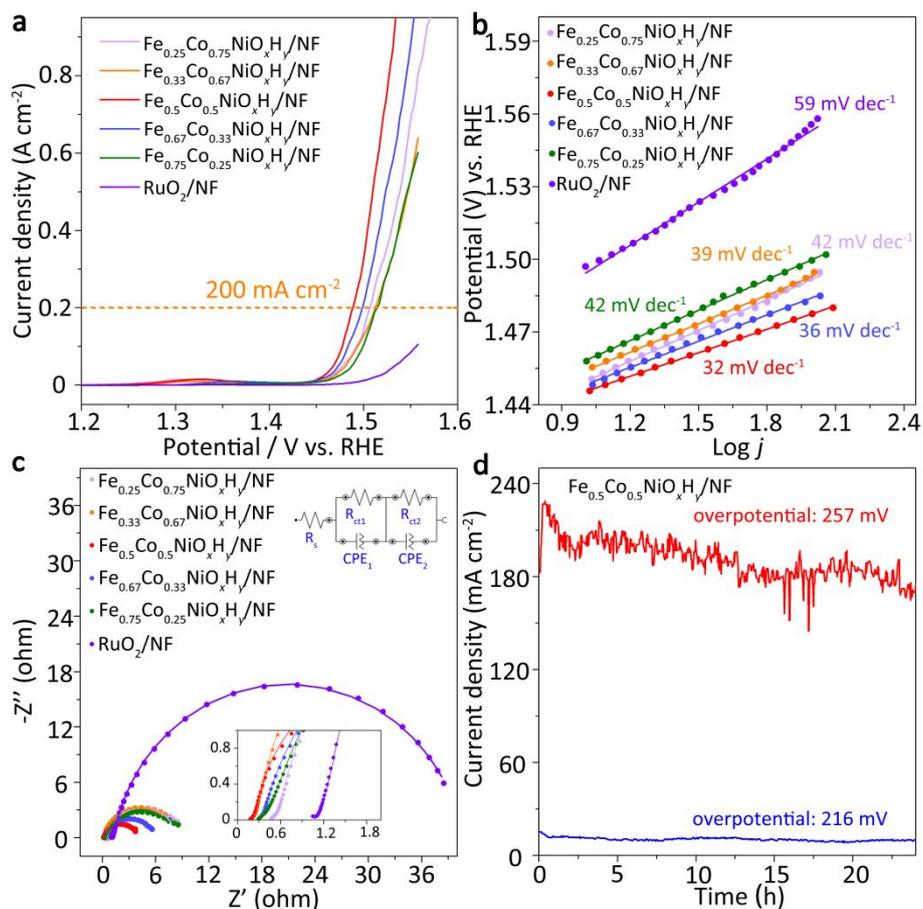
Figure 2. Electrochemical characterization of FeCoNiO$_x$H$_y$/NF with various Fe:Co:Ni ratios. (a) Polarization curves at a scan rate of 2 mV s^{-1} in 1 M KOH. (b) Tafel plots. (c) Nyquist plots. (d) Chronoamperometric measurements.

The OER kinetics on FeCoNiO$_x$H$_y$/NF and its control samples were evaluated by electrochemical impedance spectroscopy (EIS). The obtained Nyquist plots were fitted by their equivalent circuits (Figure 2c and Table S4), in which R_s is the solution resistance, R_{ct1} is the internal charge transfer resistance of NF-supported electrocatalysts (corresponding to the small semicircle in the high to middle frequency range), and R_{ct2} is the charge transfer resistance at the electrocatalyst/electrolyte interface (corresponding to the semicircles in the middle to low

frequency range) directly related to the catalytic kinetics.[36-39] Among all the electrocatalysts, FeCoNiO$_x$H$_y$/NF (Fe$_{0.5}$Co$_{0.5}$NiO$_x$H$_y$/NF) shows the lowest R_{ct1} (0.08 Ω) and R_{ct2} (3.48 Ω), which thus indicates the superior electrical conductivity and catalytic activity of FeCoNiO$_x$H$_y$/NF over all the other electrocatalysts (Table S4). <mark>Moreover, as compared with FeCoNiO$_x$H$_y$/NF, the FeCoNiO$_x$H$_y$ without NF support shows much greater R_{ct1} and R_{ct2} (3.95 and 64.1 Ω, respectively; Figure S23 and Table S4), which thus indicates the important role of NF in the electrical conductivity and catalytic activity of FeCoNiO$_x$H$_y$/NF. However, as all the FeCoNiO$_x$H$_y$/NF electrocatalysts with various Fe:Co:Ni ratios are supported on NF and compared under otherwise identical conditions, the activity difference between these FeCoNiO$_x$H$_y$/NF electrocatalysts should be attributed to their intrinsic properties other than the conductivity of NF.</mark>

The electrochemical active surface areas (ECSA) of FeCoNiO$_x$H$_y$/NF and its control samples were also calculated based on the double-layer capacitance (C_{dl}; Figure S24–29). FeCoNiO$_x$H$_y$/NF shows a C_{dl} (0.25 μF cm^{-2}) and the other trimetallic control samples (*ca.* 0.27– 30 μF cm^{-2}), implying that similar electrochemical active sites are available in FeCoNiO$_x$H$_y$/NF.

To get insights into the superior OER performances, FeCoNiO$_x$H$_y$ and its mono- and bimetallic counterparts of FeO$_x$H$_y$, CoO$_x$H$_y$, NiO$_x$H$_y$, FeNiO$_x$H$_y$, FeCoO$_x$H$_y$ and CoNiO$_x$H$_y$ are peeled off from their NF supports, and subject to XPS to reveal the chemical states of Fe, Co, and Ni and their electronic interactions (**Figure 3**). The full XPS spectrum of FeCoNiO$_x$H$_y$ confirms the presence of O, Fe, Co, and Ni elements in its structure (Figure S30). The high-resolution XPS spectrum of O verifies the existence of hydroxides in FeCoNiO$_x$H$_y$, as indicated by the peaks of M–OH (M = Fe, Co, Ni) species centered at 531.42–532.59 eV (Figure S31).[33, 40, 41] Moreover, the high-resolution XPS spectra of Fe, Co, and Ni reveal that these three elements exist in different valence states in FeCoNiO$_x$H$_y$ (Figure 3a–c and Table S5). Specifically, the deconvoluted Fe 2p spectrum show the peaks of Fe 2p$_{3/2}$ centered at 711.76 eV and Fe 2p$_{1/2}$ at 725.26 eV, which indicates that Fe exists exclusively in the form of Fe^{3+} in FeCoNiO$_x$H$_y$ (Figure 3a).[42] Similarly, Ni also exists in only one valence state of Ni^{2+}, as indicated by the Ni 2p$_{3/2}$ peak at 856.33 eV and Ni 2p$_{1/2}$ peak at 874.03 eV in the deconvoluted Ni 2p spectrum (Figure 3b).[43, 44] By contrast, the deconvoluted Co 2p spectrum clearly implies that Co exists in two valence states in FeCoNiO$_x$H$_y$: Co^{3+} indicated by the Co 2p$_{3/2}$ peak at 780.80 eV and Co 2p$_{1/2}$ peak at 795.80 eV,[35] and Co^{2+} indicated by the Co 2p$_{3/2}$ peak at 781.89 eV and the Co 2p$_{1/2}$ peak at 797.69 eV (Figure 3c).[31, 45] Fe, Co, and Ni in the control samples of FeO$_x$H$_y$, CoO$_x$H$_y$, NiO$_x$H$_y$, FeCoO$_x$H$_y$, CoNiO$_x$H$_y$ and FeNiO$_x$H$_y$ show similar valence states to that in FeCoNiO$_x$H$_y$: Fe and Ni exist in one valance state of Fe^{3+} and Ni^{2+}, respectively, while

Co exists in mixed valance states of Co^{3+} and Co^{2+} (Figure 3a–c), in line with the results reported in literature.[35, 46-48]. Moreover, different shift trends of the XPS peaks are observed for Fe, Co and Ni when comparing the tri- and bimetallic samples with their monometallic counterparts. The XPS peaks of Fe 2p, Co 2p and Ni 2p of bimetallic $CoNiO_xH_y$ and $CoFeO_xH_y$ show notable shift in binding energy (> 0.4 eV for Co, < –0.2 eV for Fe, and < –0.4 eV for Ni), implying that (1) notable electron transfer occurs from Co to Fe and Ni, (2) strong Co–Fe and Co–Ni electronic interactions exist in $CoNiO_xH_y$ and $CoFeO_xH_y$, and (3) Ni is likely to have a stronger electronic interaction with Co than Fe. In contrast, the Fe 2p and Ni 2p XPS peaks of $FeNiO_xH_y$ show minor shift (0.07 eV for Fe and –0.09 eV for Ni), suggesting much less electron transfer from Fe to Ni and accordingly much weaker Fe-Ni electronic interaction as compared with Co–Fe and Co–Ni. Moreover, trimetallic $FeCoNiO_xH_y$ shows a further positive shift in the Co^{3+} 2p peaks (0.5 eV), implying synergistic electronic interactions between Fe, Co, and Ni in $FeCoNiO_xH_y$.
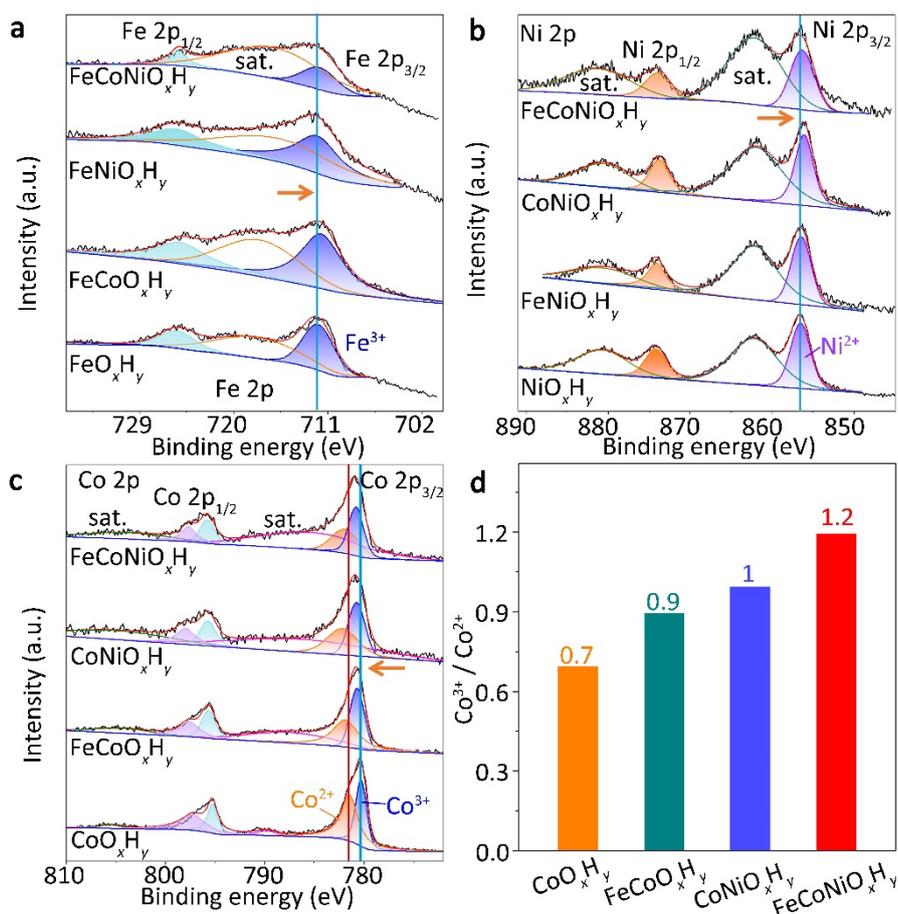
Figure 3. High-resolution XPS spectra of $FeCoNiO_xH_y$ and its control samples. (a) Fe 2p, (b) Ni 2p, (c) Co 2p, (d) Co^{3+}/Co^{2+} ratio derived from XPS spectra.

The Fe–Co–Ni electronic interactions induce a notable change in the Co^{3+}/Co^{2+} ratios in Co-containing samples. As compared with monometallic CoO_xH_y with a Co^{3+}/Co^{2+} ratio of 0.7, the presence of a second metal of Fe and Ni increases the Co^{3+}/Co^{2+} ratio to 0.9 for $FeCoO_xH_y$ and 1.0 for $CoNiO_xH_y$, respectively. The addition of both Fe and Ni to Co further notably increases the Co^{3+}/Co^{2+} ratio to 1.2 for $FeCoNiO_xH_y$. These results suggest that Ni induces a greater Co^{3+}/Co^{2+} ratio than Fe, and Fe and Ni synergistically induce a further increased Co^{3+}/Co^{2+} ratio. In fact, the Co^{3+}/Co^{2+} ratios change in the same way as the binding energy shift of the Co^{3+} 2p XPS peaks in corresponding samples (Figure 3a–c and Table S5), which suggests that higher Co^{3+}/Co^{2+} ratio could be induced by larger binding energy shift of the Co^{3+} 2p XPS peaks, and vice versa. The variation of Co^{3+}/Co^{2+} ratios and binding energy shift of Co^{3+} 2p XPS peaks thus collectively confirm the synergistic electronic interactions between Fe, Co and Ni, by which the redox activity of Co in bi- and trimetallic Co-containing electrocatalysts can be "activated" and thus more Co^{3+} are formed before OER.[31]
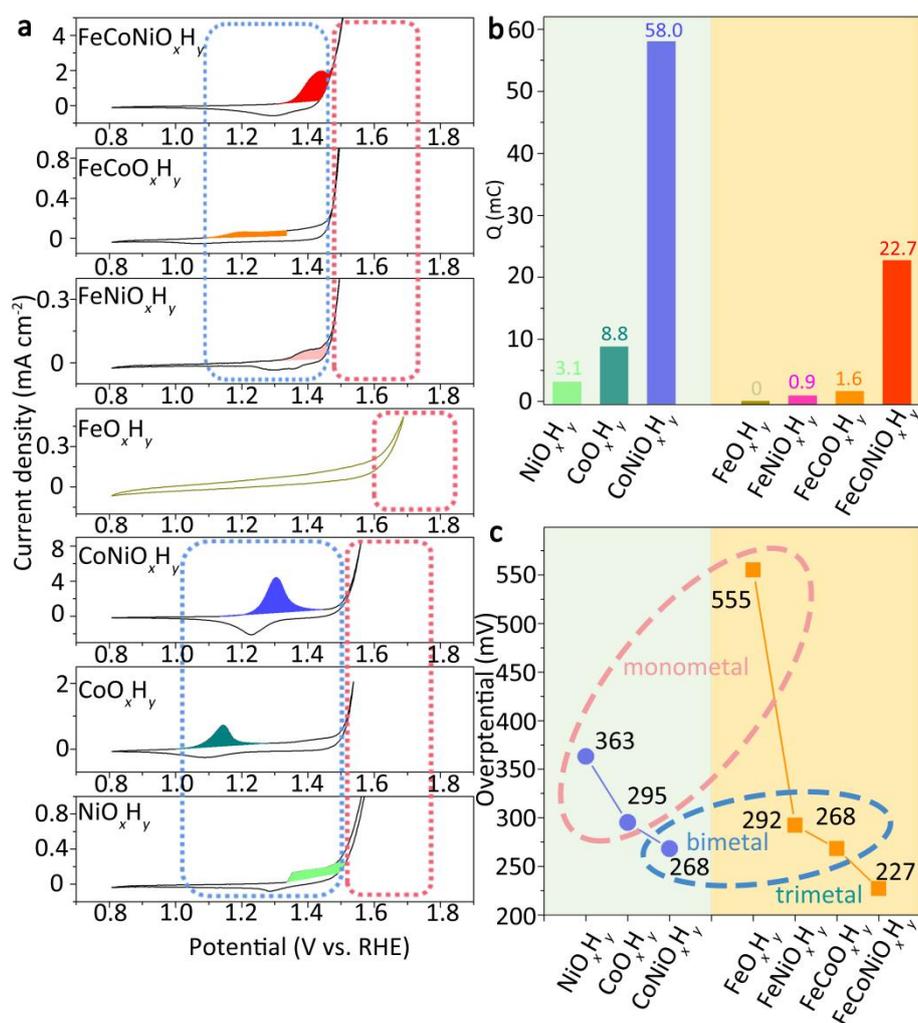
Figure 4. (a) CV curves, (b) anodic peak charges, and (c) overpotentials of $FeCoNiO_xH_y$ and its mono- and bimetallic counterparts.

Cyclic voltammetry (CV) was also applied to trimetallic $FeCoNiO_xH_y$ and its mono- and bimetallic counterparts to reveal the impacts of electronic interactions on the electrochemical properties of Fe, Co, and Ni during OER. The CV curves of all samples were collected after seven LSV cycles (**Figure 4** and Figure S32–33; to avoid the disturbance in understanding the electrochemical nature of Fe, Co, and Ni caused by the electrochemical oxidation of NF backbones, all the electrocatalyst powders were deposited on glassy carbon electrodes and tested at a scan rate of 5 mV s^{-1}). Notably, all the samples except FeO_xH_y show only one pair of redox peaks in their corresponding CV curves in the large potential range of 0.8–1.6 V vs RHE, and the redox peak pairs differentiate from each other in not only peak position but also peak area. As demonstrated in literature,[23, 49] the integrated area of redox peaks is indicative of the extent of redox process of metal catalyst, and thus the quantity of electric charge associated with the anodic peak in each CV curve (anodic peak charge), Q, is used to evaluate the redox activity of metal catalysts (Figure 4b). The monometallic NiO_xH_y displays a pair of Ni^{2+}/Ni^{3+} redox peaks at 1.37 V (anodic) and 1.30 V (cathodic),[48, 50] with a small anodic peak charge of 3.1 mC. By comparison, the monometallic CoO_xH_y manifests a pair of Co^{2+}/Co^{3+} redox peaks at lower potential of 1.16 V (anodic) and 1.11 V (cathodic),[51-53] and with a much larger peak charge of 8.8 mC. Such difference suggests that, as compared with Ni, Co has a higher M^{2+}/M^{3+} redox activity and thus the generation of high-valence Co^{3+} is facilitated during the OER process. The CV curve of $CoNiO_xH_y$ show a redox peak pair locate in between that of CoO_xH_y and NiO_xH_y, which could be ascribed to the M^{2+}/M^{3+} redox process of Co and Ni. Remarkably, the peak charge of bimetallic $CoNiO_xH_y$ sharply increases to 58.0 mC, far higher than that of monometallic CoO_xH_y and NiO_xH_y, indicating that notable synergistic electronic interaction exists between Co and Ni,[54, 55] and much more high-valence M^{3+} in the form of oxyhydroxides are generated on the surface of $CoNiO_xH_y$.[8, 40, 56, 57] The notable synergistic electronic interaction between Co and Ni in $CoNiO_xH_y$ can be further supported by the appearance of only one redox peak pair in the CV curve, rather than two independent redox peak pairs that correspond to the M^{2+}/M^{3+} redox process of Co and Ni, respectively.[35, 58] It is worth noting that the redox peak pairs of Co^{3+}/Co^{4+} in CoO_xH_y and Ni^{3+}/Ni^{4+} in NiO_xH_y are not observed in their corresponding CV curves, which are likely to be postponed and appear together with the OER current rising.[51]

The FeO_xH_y, however, exhibits a typical capacitive current without any redox features or anodic peak charge in the potential range of 0.8 to 1.6 V vs RHE (Figure 4a,b), and a Faradic current peak associated with OER only occurs at potential higher than 1.6 V, which is similar to the results reported previously.[21, 22, 59] Therefore, Fe largely remains in the initial valence

13

state of Fe^{3+} before the Faradic current peak occur.[24] When doped with Co or Ni, the CV curves of bimetallic $FeCoO_xH_y$ and $FeNiO_xH_y$ also show a pair of redox peak locating at higher potential level than CoO_xH_y and NiO_xH_y, respectively, which is indicative of the Fe–Co and Fe–Ni electronic interactions. However, the anodic peak charge of $FeCoO_xH_y$ and $FeNiO_xH_y$ decreases sharply as compared with their monometallic counterparts of CoO_xH_y and NiO_xH_y. The trimetallic $FeCoNiO_xH_y$ also follows similar trend as compared with its counterpart without Fe, i.e., $CoNiO_xH_y$. The Fe–induced sharp decrease in anodic peak charge indicates that the M^{2+}/M^{3+} redox process is significantly hindered by Fe, in line with the previously reported observation that the electrochemical oxidation of Co^{2+} and Ni^{2+} to Co^{3+} and Ni^{3+} , respectively, can be notably suppressed in the presence of Fe^{3+}.[24, 25, 59] It is worth noting that the CV curves and XPS spectra seem to give contradictory clues to the Fe–Co interaction in $FeCoO_xH_y$ and $FeCoNiO_xH_y$: Fe^{3+} is found to significantly suppresses the electrochemical oxidation of Co^{2+} to Co^{3+} in the CV curves but notably facilitate the formation of more high-valence Co^{3+} in the XPS spectra (cf. Figure 3–4). Such observation should be attributed to different test conditions of CV and XPS. XPS spectra shows the intrinsic Fe–Co interaction under no applied potential, while CV curves presents the further change in the Fe–Co interaction when the electrocatalysts are tested in 1 M KOH and under applied potential. Therefore, the CV results reflect the suppressed oxidation of remaining Co^{2+} in electrocatalysts, likely due to the strong binding affinity between Fe^{3+} in electrocatalysts and OH^- in electrolyte, by which stable OH^- adlayer forms on electrocatalyst surface, greatly blocks the surface Co^{2+} sites and thus significantly decreases the redox activity of Co^{2+}.[60] For similar reason, sharp decline in anodic peak charge is also observed for Fe-containing electrocatalysts when compared with their counterparts without Fe (Figure 4b).

Moreover, it is interesting to find that the anodic peak charge correlates well with the overpotential (at a current density of 1.5 mA cm^{-2}) for (1) the Co-and Ni-electrocatalysts without Fe, and (2) the Co- and Ni-electrocatalysts with Fe (Figure 4b,c). The OER overpotential decreases from 363 mV for NiO_xH_y to 295 mV for CoO_xH_y and further to 268 mV for $CoNiO_xH_y$ as the corresponding anodic peak charge increases from 3.1 to 8.8 and 58.0 mC. Meanwhile, the OER overpotential decreases from 555 mV for FeO_xH_y to 292 mV for $FeNiO_xH_y$, 268 mV for $FeCoO_xH_y$, and finally to 227 mV for $FeCoNiO_xH_y$ as the corresponding anodic peak charge increases from 0 to 0.9, 1.6 and 22.7 mC. Such anodic peak charge–overpotential relationship suggests that intrinsic redox activity of metal ions and the synergistic electronic interaction between different metals play a critical role in the OER activity of electrocatalysts. However, we also notice that the Fe-doped Co- and Ni-electrocatalysts show

substantially lowered overpotential despite their much smaller andic peak charge as compared with their counterparts without Fe. For instance, $CoNiO_xH_y$ with an anodic peak charge of 58.0 mC delivers an overpotential of 268 mV while $FeCoNiO_xH_y$ with an anodic peak charge of 22.7 mC deliver an overpotential of 227 mV. These results indicate that despite the very poor redox activity, Fe is also capable of contributing remarkably to the superior OER activity of $FeCoNiO_xH_y$ and thus additional factor should be taken into account to rationalize the contribution of Fe.
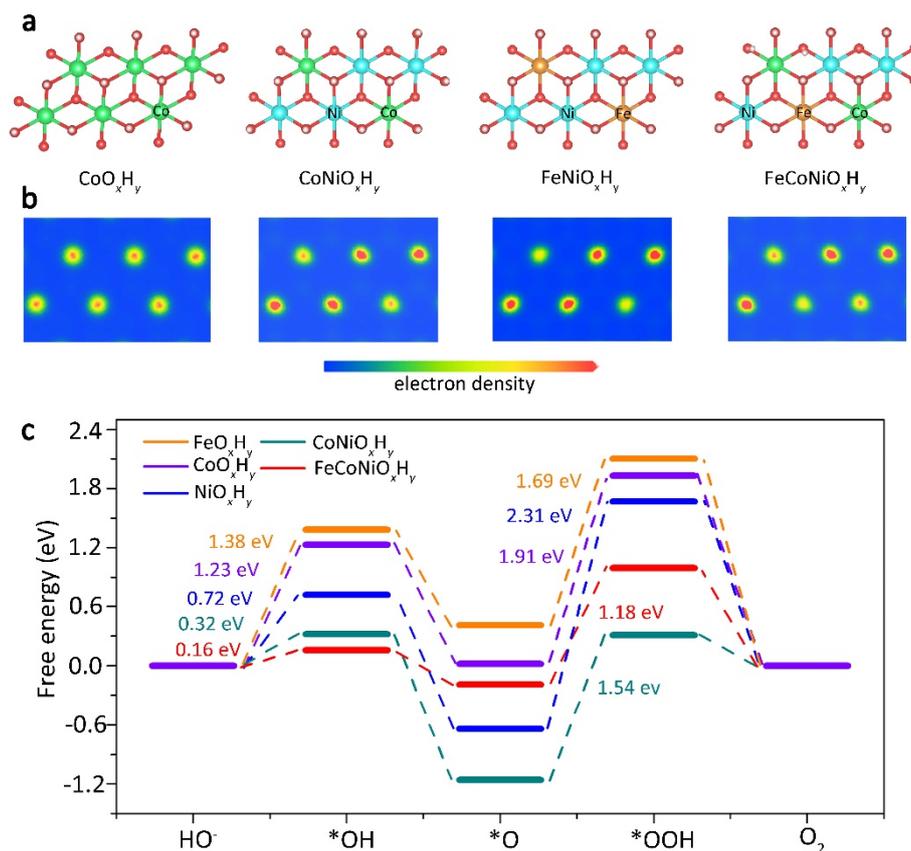
Figure 5. DFT calculations-based theoretical analysis of OER on representative catalysts. (a) Structure models, (b) electron density around metal sites, and (c) Gibbs free energy diagrams.

To gain further insights into the roles of Fe, Co, and Ni in OER activity, the Gibbs free energies of the reactions involved in OER were calculated, based on density functional theory (DFT) and the four-electron OER mechanism under alkaline condition:[61-63]

ΔG_1 $\quad\quad\quad$ $* + OH^- \rightarrow *OH + e^-$ $\quad\quad\quad\quad\quad\quad\quad\quad\quad\quad\quad\quad$ (1)

ΔG_2 $\quad\quad\quad$ $*OH + OH^- \rightarrow *O + H_2O + e^-$ $\quad\quad\quad\quad\quad\quad\quad\quad$ (2)

ΔG_3 $\quad\quad\quad$ $*O + OH^- \rightarrow *OOH + e^-$ $\quad\quad\quad\quad\quad\quad\quad\quad\quad\quad$ (3)

ΔG_4 $\quad\quad\quad$ $*OOH + OH^- \rightarrow O_2 + H_2O + e^-$ $\quad\quad\quad\quad\quad\quad\quad$ (4)
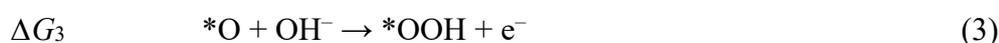
where the structure models of representative electrocatalysts of CoO_xH_y, $CoNiO_xH_y$, $FeNiO_xH_y$, and $FeCoNiO_xH_y$ are shown in **Figure 5**a, and * denotes the active site of electrocatalysts. After structure/energy stabilization and optimization, the electron density around metal ions and the Gibbs free energies for each elemental reaction are obtained (Figure 5b,c). As compared with monometallic CoO_xH_y, the electron density around Co clearly decreases in bimetallic $CoNiO_xH_y$ and trimetallic $FeCoNiO_xH_y$, and as compared with $FeNiO_xH_y$, the electron density around Fe and Ni in $FeCoNiO_xH_y$ clearly increases due to the electron transfer from Co to Fe and Ni (Figure 5a,b). These results are consistent with the XPS results (Figure 3) and thus further confirms the electronic interactions between Fe, Co and Ni. Moreover, the Gibbs free energy associated with the formation of *OOH intermediates, ΔG_3, is larger than the other three for all the electrocatalysts (Figure 5c), implying that the *OOH formation reaction is the RDS (rate-determining step) of OER.[62]

Among the three monometallic electrocatalysts, it is interesting to note that FeO_xH_y has the lowest ΔG_3 (1.69 eV) as compared with CoO_xH_y (1.91 eV) and NiO_xH_y (2.31 eV), which suggests that FeO_xH_y should have the highest catalytic activity and lowest overpotential, in line with previously reported results.[21, 22, 55] However, our experimental data shows that FeO_xH_y delivers the lowest apparent activity, as indicated by its highest overpotential (555 mV; Figure 4c). Moreover, the highest ΔG_3 (2.31 eV) of NiO_xH_y is expected to result in the highest overpotential, which, however, is again inconsistent with our experimental observation (Figure 4c). In fact, similar observation regarding the inconsistency between theoretical and experimental results has also been reported and rationalized for bimetallic OER electrocatalysts of Fe–Co and Fe–Ni oxyhydroxides,[19, 21, 22] which confirms the superior intrinsic activity but inferior apparent activity of FeO_xH_y over CoO_xH_y and NiO_xH_y, and further attributes the inconsistency between theoretical and experimental results to the notable difference in the electrical conductivity of oxyhydroxides generated during OER. Good intrinsic conductivity enables OER-associated current to flow across electrocatalyst at low overpotential, which benefits the charge transfer across electrocatalyst, allows for the efficient activation of abundant catalytic sites throughout electrocatalysts, and finally leads to high apparent OER activity. By *in situ* measurement, the electrical conductivity of FeO_xH_y, NiO_xH_y, and CoO_xH_y was found to be *ca*. 0.02, 0.1 – 0.2, and 4.5 mS cm^{-1}, respectively.[19, 21, 22] As compared with NiO_xH_y and CoO_xH_y, FeO_xH_y with far inferior conductivity requires much higher potential to drive the OER-associated current across electrocatalyst and thus shows much lower apparent OER activity, despite its higher intrinsic catalytic activity. In a similar way, the observed apparent OER activity (indicated by overpotential) of other mono-, bi-, and trimetallic electrocatalysts in our

work can be well interpreted by taking both the intrinsic activity (indicated by ΔG_3 derived from DFT calculations) and electrical conductivity into account. Among monometallic electrocatalysts, CoO_xH_y has moderate intrinsic activity (indicated by its moderate ΔG_3) but far superior conductivity over FeO_xH_y and NiO_xH_y, and thus show the lowest potential; NiO_xH_y has the lowest, but not way worst intrinsic activity and moderate conductivity, and therefore delivers moderate overpotential.

As compared with monometallic electrocatalysts, the bi- and trimetallic electrocatalysts show much smaller ΔG_3, which is indicative of remarkably improved intrinsic activity and notable synergistic effect between different metals. As a typical example, ΔG_3 sharply decreases from 2.31 and 1.91 eV for monometallic NiO_xH_y and CoO_xH_y, respectively, to 1.54 eV for bimetallic $CoNiO_xH_y$, and further to 1.18 eV for trimetallic $FeCoNiO_xH_y$ (Figure 5c). In addition, the decreasing trend of ΔG_3 is in line with that of overpotential (apparent OER activity) in our experiments, from 363 and 295mV for monometallic NiO_xH_y and CoO_xH_y, respectively, to 268 mV for bimetallic $CoNiO_xH_y$, and further to 227 mV for trimetallic $FeCoNiO_xH_y$. From this point of view, ΔG_3 plays a critical role in the apparent OER activity of bi- and trimetallic electrocatalysts. However, the contribution of electrical conductivity should not be ignored. As compared with CoO_xH_y, $CoNiO_xH_y$ and $FeCoNiO_xH_y$ have higher Co^{3+}/Co^{2+} ratio at initial state (Figure 3d) and much more Co^{3+} that can be further generated under applied potential, as indicated by the larger anodic peak areas in the CV curves (Figure 4a,b). The formation of abundant Co^{3+} in the form of highly conductive Co oxyhydroxide should lead to significantly improved conductivity of $CoNiO_xH_y$ and $FeCoNiO_xH_y$, which significantly facilitates the charge transfer and catalytic site activation throughout electrocatalyst and in turn remarkably enhances the apparent OER activity of $CoNiO_xH_y$ and $FeCoNiO_xH_y$.

Based on all the above discussion, we propose a plausible mechanism to rationalize the excellent OER activity of $FeCoNiO_xH_y$. As illustrated in Scheme 1c, Fe^{3+} is the most active site for the formation of *OOH intermediates, the RDS of OER. The synergistic electronic interaction between Fe, Co, and Ni further increases the intrinsic OER activity, by endowing $FeCoNiO_xH_y$ with very low ΔG_3 for the formation of *OOH intermediates. Meanwhile, Fe^{3+} and Ni^{2+} withdraw electrons from Co^{2+} to facilitate the formation of abundant Co^{3+} that contributes predominantly to the intrinsic electrical conductivity of $FeCoNiO_xH_y$ due to the far superior conductivity of Co oxyhydroxide over Ni and Fe oxyhydroxides. The synergistic Fe–Co–Ni electronic interaction not only results in high Co^{3+}/Co^{2+} ratio in $FeCoNiO_xH_y$ but also enables the generation of many additional Co^{3+} under applied OER potential. In such a way, the intrinsic conductivity of $FeCoNiO_xH_y$ can be remarkably enhanced to benefit the charge

transfer across electrocatalyst and also the efficient activation of catalytic sites throughout electrocatalysts, and thus the poor conductivity issue induced by the Fe^{3+}-suppressed oxidation of M^{2+} to M^{3+}, which is observed for bimetallic Fe–Co and Fe–Ni electrocatalysts in our work and in literature,[24, 25, 59] can be effectively avoided. The collaborative coupling of notably enhanced intrinsic activity and conductivity allows for substantially accelerated OER kinetics at lower potential, finally leading to the superior apparent activity (indicated by the ultra-low OER overpotential) for $FeCoNiO_xH_y$.

3. Conclusion

In summary, trimetallic $FeCoNiO_xH_y$ electrocatalyst with nanotubular structure and poor crystallinity nature was synthesized by the *in situ* electrochemical oxidation of FeCoNi-MOF-74 in alkaline electrolyte, and the formation process of $FeCoNiO_xH_y$ could be interpreted as a consequence of enhanced Kirkendall effect under applied potential. The synergistic electronic interaction between Fe, Co, and Ni notably increases the intrinsic OER activity of $FeCoNiO_xH_y$ by substantially decreasing the Gibbs free energy for the formation of *OOH intermediate, the RDS of OER. The synergistic Fe-Co-Ni electronic interaction also remarkably improves the intrinsic conductivity of $FeCoNiO_xH_y$ to promote the charge transfer and catalytic site activation throughout electrocatalyst, by benefiting the formation of abundant Co^{3+}. In such a way, the high intrinsic OER activity of Fe^{3+} and high electrical conductivity of Co^{3+} oxyhydroxide are properly integrated in $FeCoNiO_xH_y$. The collaborative coupling of significantly enhanced conductivity and activity leads to substantially accelerated OER kinetics at much lower potential, finally leading to the superior apparent activity for $FeCoNiO_xH_y$. When tested in 1 M KOH electrolyte, $FeCoNiO_xH_y$ is capable of delivering an ultra-low overpotential of 257 mV at a high current density of 200 mA cm^{-2}, which ranks our $FeCoNiO_xH_y$ among the best Fe, Co, and Ni-based electrocatalysts developed so far. Our work provides new insights into the development of advanced multicomponent/multifunctional electrocatalysts for highly efficient energy conversion technology and devices.

Supporting Information

Supporting Information is available from the Wiley Online Library or from the author.

Conflict of Interest

The authors declare no conflict of interest.

References

[1]   X. S. Wang, A. Vasileff, Y. Jiao, Y. Zheng, S. Z. Qiao, *Adv. Mater.* **2019**, 31, 1803625.

[2]   S. L. Zhao, Y. C. Yang, Z. Y. Tang, *Angew. Chem., Int. Ed.* **2022**, 61, e202110186.

[3]   M. Chatenet, B. G. Pollet, D. R. Dekel, F. Dionigi, J. Deseure, P. Millet, R. D. Braatz, M. Z. Bazant, M. Eikerling, I. Staffell, P. Balcombe, Y. Shao-Horn, H. Schafer, *Chem. Soc. Rev.* **2022**, 51, 4583.

[4]   X. P. Tao, Y. Zhao, S. Y. Wang, C. Li, R. G. Li, *Chem. Soc. Rev.* **2022**, 51, 3561.

[5]   M. Z. Rahman, C. W. Kwong, K. Davey, S. Z. Qiao, *Energy Environ. Sci.* **2016**, 9, 709.

[6]   X. H. Xie, L. Du, L. T. Yon, S. Y. Park, Y. Qiu, J. Sokolowski, W. Wang, Y. Y. Shao, *Adv. Funct. Mater.* **2022**, 32, 202110036.

[7]   M. Q. Yu, E. Budiyanto, H. Tuysuz, *Angew. Chem., Int. Ed.* **2022**, 61, e202103824.

[8]   H.-Y. Wang, Y.-Y. Hsu, R. Chen, T.-S. Chan, H. M. Chen, B. Liu, *Adv. Energy Mater.* **2015**, 5, 1500091.

[9]   Y. He, X. Liu, G. Chen, J. Pan, A. Yan, A. Li, X. Lu, D. Tang, N. Zhang, T. Qu, R. Ma, T. Sasaki, *Chem. Mater.* **2020**, 32, 4232.

[10]   R. Gao, D. P. Yan, *Adv. Energy Mater.* **2020**, 10, 1900954.

[11]   C. Feng, M. B. Faheem, J. Fu, Y. Q. Xiao, C. L. Li, Y. B. Li, *ACS Catal.* **2020**, 10, 4019.

[12]   F. Dionigi, Z. H. Zeng, I. Sinev, T. Merzdorf, S. Deshpande, M. B. Lopez, S. Kunze, I. Zegkinoglou, H. Sarodnik, D. X. Fan, A. Bergmann, J. Drnec, J. F. de Araujo, M. Gliech,

19

D. Teschner, J. Zhu, W. X. Li, J. Greeley, B. Roldan Cuenya, P. Strasser, *Nat. Commun.* **2020**, 11, 2522.

[13]   H. Xiao, H. Shin, W. A. Goddard, *Proc. Natl. Acad. Sci. U. S. A.* **2018**, 115, 5872.

[14]   D. Yu, Y. Ma, F. Hu, C.-C. Lin, L. Li, H.-Y. Chen, X. Han, S. Peng, *Adv. Energy Mater.* **2021**, 11, 2101242.

[15]   X. Zhang, Y. Zhao, Y. Zhao, R. Shi, G. I. N. Waterhouse, T. Zhang, *Adv. Energy Mater.* **2019**, 9, 1900881.

[16]   F. Q. Zheng, W. F. Zhang, X. X. Zhang, Y. L. Zhang, W. Chen, *Adv. Funct. Mater.* **2021**, 31, 2103318.

[17]   H. X. Liao, T. Luo, P. F. Tan, K. J. Chen, L. L. Lu, Y. Liu, M. Liu, J. Pan, *Adv. Funct. Mater.* **2021**, 31, 2102772.

[18]   N.-T. Suen, S.-F. Hung, Q. Quan, N. Zhang, Y.-J. Xu, H. M. Chen, *Chem. Soc. Rev.* **2017**, 46, 337.

[19]   L. Trotochaud, S. L. Young, J. K. Ranney, S. W. Boettcher, *J. Am. Chem. Soc.* **2014**, 136, 6744.

[20]   B. S. Yeo, A. T. Bell, *J. Am. Chem. Soc.* **2011**, 133, 5587.

[21]   M. S. Burke, M. G. Kast, L. Trotochaud, A. M. Smith, S. W. Boettcher, *J. Am. Chem. Soc.* **2015**, 137, 3638.

[22]   M. S. Burke, S. H. Zou, L. J. Enman, J. E. Kellon, C. A. Gabor, E. Pledger, S. W. Boettcher, *J. Phys. Chem. Lett.* **2015**, 6, 3737.

[23]   X. Zhang, F. Yan, X. Z. Ma, C. L. Zhu, Y. Wang, Y. Xie, S. L. Chou, Y. J. Huang, Y. J. Chen, *Adv. Energy Mater.* **2021**, 11, 2102141.

[24]   M. Goerlin, P. Chernev, J. F. de Araujo, T. Reier, S. Dresp, B. Paul, R. Kraehnert, H. Dau, P. Strasser, *J. Am. Chem. Soc.* **2016**, 138, 5603.

[25]   M. Goerlin, J. F. de Araujo, H. Schmies, D. Bernsmeier, S. Dresp, M. Gliech, Z. Jusys, P. Chernev, R. Kraehnert, H. Dau, P. Strasser, *J. Am. Chem. Soc.* **2017**, 139, 2070.

[26]   L. J. Wang, H. Deng, H. Furukawa, F. Gandara, K. E. Cordova, D. Peri, O. M. Yaghi, *Inorg. Chem.* **2014**, 53, 5881.

[27]   X. L. Wang, H. Xiao, A. Li, Z. Li, S. J. Liu, Q. H. Zhang, Y. Gong, L. R. Zheng, Y. Q. Zhu, C. Chen, D. S. Wang, Q. Peng, L. Gu, X. D. Han, J. Li, Y. D. Li, *J. Am. Chem. Soc.* **2018**, 140, 15336.

[28]   D. Zhou, J. Ni, L. Li, *Nano Energy* **2019**, 57, 711.

[29]   F. Sun, G. Wang, Y. Ding, C. Wang, B. Yuan, Y. Lin, *Adv. Energy Mater.* **2018**, 8, 1800584.

[30] J. Xing, K. Guo, Z. Zou, M. Cai, J. Du, C. Xu, *Chem. Commun.* **2018**, 54, 7046.

[31] H. Sun, L. Chen, Y. Lian, W. Yang, L. Lin, Y. Chen, J. Xu, D. Wang, X. Yang, M. H. Rummerli, J. Guo, J. Zhong, Z. Deng, Y. Jiao, Y. Peng, S. Qiao, *Adv. Mater.* **2020**, 32, 2006784.

[32] X. Xu, F. Song, X. L. Hu, *Nat. Commun.* **2016**, 7, 7.

[33] M. Q. Chen, Y. Y. Xie, J. X. Wu, H. F. Huang, J. Teng, D. W. Wang, Y. N. Fan, J. J. Jiang, H. P. Wang, C. Y. Su, *J. Mater. Chem. A* **2019**, 7, 10217.

[34] W. Wang, M. Dahl, Y. Yin, *Chem. Mater.* **2013**, 25, 1179.

[35] W. X. Wang, Y. Lu, M. L. Zhao, R. J. Luo, Y. Yang, T. Peng, H. L. Yan, X. M. Liu, Y. S. Luo, *ACS Nano* **2019**, 13, 12206.

[36] Y. Teng, X. D. Wang, J. F. Liao, W. G. Li, H. Y. Chen, Y. J. Dong, D. B. Kuang, *Adv. Funct. Mater.* **2018**, 28, 1802463.

[37] J. Jiang, F. Sun, S. Zhou, W. Hu, H. Zhang, J. Dong, Z. Jiang, J. Zhao, J. Li, W. Yan, M. Wang, *Nat. Commun.* **2018**, 9, 2285.

[38] Y. Xie, M. Chen, M. Cai, J. Teng, H. Huang, Y. Fan, M. Barboiu, D. Wang, C.-Y. Su, *Inorg. Chem.* **2019**, 58, 14652.

[39] Y. Xie, H. Huang, Z. Chen, Z. He, Z. Huang, S. Ning, Y. Fan, M. Barboiu, J.-Y. Shi, D. Wang, C.-Y. Su, *Inorg. Chem.* **2022**, 61, 8283.

[40] D. Zhou, S. Wang, Y. Jia, X. Xiong, H. Yang, S. Liu, J. Tang, J. Zhang, D. Liu, L. Zheng, Y. Kuang, X. Sun, B. Liu, *Angew. Chem., Int. Ed.* **2019**, 58, 736.

[41] W. Hu, Y. Liu, R. L. Withers, T. J. Frankcombe, L. Noren, A. Snashall, M. Kitchin, P. Smith, B. Gong, H. Chen, J. Schiemer, F. Brink, J. Wong-Leung, *Nat. Mater.* **2013**, 12, 821.

[42] M. Zhang, Y. Liu, B. Liu, Z. Chen, H. Xu, K. Yan, *ACS Catal.* **2020**, 10, 5179.

[43] S. A. Chala, M.-C. Tsai, W.-N. Su, K. B. Ibrahim, B. Thirumalraj, T.-S. Chan, J.-F. Lee, H. Dai, B.-J. Hwang, *ACS Nano* **2020**, 14, 1770.

[44] J. Chen, F. Zheng, S.-J. Zhang, A. Fisher, Y. Zhou, Z. Wang, Y. Li, B.-B. Xu, J.-T. Li, S.-G. Sun, *ACS Catal.* **2018**, 8, 11342.

[45] Y. Q. Guo, X. F. Hong, Y. Wang, Q. Li, J. S. Meng, R. T. Dai, X. Liu, L. He, L. Q. Mai, *Adv. Funct. Mater.* **2019**, 29, 1809004.

[46] L. Zhuang, L. Ge, Y. Yang, M. Li, Y. Jia, X. Yao, Z. Zhu, *Adv. Mater.* **2017**, 29, 1606793.

[47] L. Gong, X. Y. E. Chng, Y. Du, S. Xi, B. S. Yeo, *ACS Catal.* **2018**, 8, 807.

[48] Q. Zhou, Y. Chen, G. Zhao, Y. Lin, Z. Yu, X. Xu, X. Wang, H. K. Liu, W. Sun, S. X. Dou, *ACS Catal.* **2018**, 8, 5382.

[49] H. B. Tao, L. Fang, J. Chen, H. B. Yang, J. Gao, J. Miao, S. Chen, B. Liu, *J. Am. Chem. Soc.* **2016**, 138, 9978.

[50] A. Dutta, S. Mutyala, A. K. Samantara, S. Bera, B. K. Jena, N. Pradhan, *ACS Energy Lett.* **2018**, 3, 141.

[51] H.-Y. Wang, S.-F. Hung, H.-Y. Chen, T.-S. Chan, H. M. Chen, B. Liu, *J. Am. Chem. Soc.* **2016**, 138, 36.

[52] A. Moysiadou, S. Lee, C.-S. Hsu, H. M. Chen, X. Hu, *J. Am. Chem. Soc.* **2020**, 142, 11901.

[53] A. Bergmann, T. E. Jones, E. M. Moreno, D. Teschner, P. Chernev, M. Gliech, T. Reier, H. Dau, P. Strasser, *Nat. Catal.* **2018**, 1, 711.

[54] Y. Y. Liu, X. Teng, Y. L. Mi, Z. F. Chen, *J. Mater. Chem. A* **2017**, 5, 24407.

[55] M. K. Bates, Q. Jia, H. Doan, W. Liang, S. Mukerjee, *ACS Catal.* **2016**, 6, 155.

[56] A. Sivanantham, P. Ganesan, A. Vinu, S. Shanmugam, *ACS Catal.* **2020**, 10, 463.

[57] W. J. Liu, X. Hu, H. C. Li, H. Q. Yu, *Small* **2018**, 14, 11.

[58] Q. H. Zhao, J. L. Yang, M. Q. Liu, R. Wang, G. X. Zhang, H. Wang, H. T. Tang, C. K. Liu, Z. W. Mei, H. B. Chen, F. Pan, *ACS Catal.* **2018**, 8, 5621.

[59] M. W. Louie, A. T. Bell, *J. Am. Chem. Soc.* **2013**, 135, 12329.

[60] R. Subbaraman, D. Tripkovic, K. C. Chang, D. Strmcnik, A. P. Paulikas, P. Hirunsit, M. Chan, J. Greeley, V. Stamenkovic, N. M. Markovic, *Nat. Mater.* **2012**, 11, 550.

[61] H. Fei, J. Dong, Y. Feng, C. S. Allen, C. Wan, B. Volosskiy, M. Li, Z. Zhao, Y. Wang, H. Sun, P. An, W. Chen, Z. Guo, C. Lee, D. Chen, I. Shakir, M. Liu, T. Hu, Y. Li, A. I. Kirkland, X. Duan, Y. Huang, *Nat. Catal.* **2018**, 1, 63.

[62] K. Shah, R. Y. Dai, M. Mateen, Z. Hassan, Z. W. Zhuang, C. H. Liu, M. Israr, W. C. Cheong, B. T. Hu, R. Y. Tu, C. Zhang, X. Chen, Q. Peng, C. Chen, Y. D. Li, *Angew. Chem., Int. Ed.* **2022**, 61, e202114951.

[63] Y. Jiao, Y. Zheng, M. Jaroniec, S. Z. Qiao, *J. Am. Chem. Soc.* **2014**, 136, 4394.